Phys Chem Minerals (2003) 30: 20–30
DOI 10.1007/s00269-002-0287-x

ORIGINAL PAPER

F. Cámara · G. Iezzi · R. Oberti

H*T*-XRD study of synthetic ferrian magnesian spodumene: the effect of site dimension on the $P2_1/c \rightarrow C2/c$ phase transition

Received: 7 May 2002 / Accepted: 23 October 2002

Abstract Ferrian magnesian spodumene was synthesized in the MLFSH system at $P = 0.4$ GPa, $T = 700$ °C, $fO_2 = \mathrm{NNO} + 2.3$. The space group at room T is $P2_1/c$ [$a = 9.638(3)$ Å, $b = 8.709(2)$ Å, $c = 5.258(2)$ Å, $\beta = 109.83(3)^\circ$, $V = 415.2$ Å^3]. The structure is topologically equivalent to that of ferrian spodumene, $LiFeSi_2O_6$, and has two symmetrically independent tetrahedral chains, A and B, and two independent octahedral sites, M1 and M2. The crystal-chemical composition was determined combining EMP, SIMS and single-crystal XRD analysis, yielding $^{M2}(Li_{0.85}Mg_{0.09}Fe^{2+}_{0.06})\ ^{M1}(Fe^{3+}_{0.85}Mg_{0.15})Si_2O_6$. Li is ordered at the M2 site and Fe^{3+} is ordered at the M1 site, whereas Mg (and Fe^{2+}) distribute over both octahedral sites. Structure refinements done at different temperatures (25, 70, 95, 125, 150 and 200 °C) allowed characterization of a reversible displacive $P2_1/c \rightarrow C2/c$ transition at 106 °C. Previous H*T*-XRD studies of Li-clinopyroxenes had shown that the transition temperature is inversely related to the size of the M1 cation. For the crystal of this work, the aggregate ionic radius at M1 is longer than that of ferrian spodumene, for which the transition temperature is −44 °C. The higher transition temperature observed can only be explained on the basis of the shorter aggregate radius at the M2 site (due to the presence of Mg substituting after Li), in keeping with the results obtained for ferromagnesian $P2_1$/c pyroxenes. The effects of all the chemical substitutions must be considered when modelling transition temperatures and thermodynamic behaviour in clinopyroxenes.

Keywords Li–clinopyroxene · Displacive phase–transition · H*T*–XRD · Synthesis

Electronic Supplementary Material. Tables 4 and 6 have been deposited in electronic form and can be obtained from http://link.springer.de/link/service/journals/00269

F. Cámara (✉) · R. Oberti
CNR-Istituto di Geoscienze e Georisorse,
sezione di Pavia, via Ferrata 1, 27100 Pavia
e-mail: camara@crystal.unipv.it
Tel.: +39 0382 505867
Fax: +39 0382 505887

G. Iezzi
Dipartimento di Scienze della Terra,
Università G. D'Annunzio, 66013 Chieti Scalo

G. Iezzi
ISTO-CNRS, 1A, Rue de la Ferollerie,
45071, Orléans CEDEX 2, France

Introduction

Several synthetic Li-clinopyroxenes have already been characterized by single-crystal X-ray structure refinement. Most of them have the $C2/c$ space group at room temperature. At lower temperature, the space group is $P2_1/c$, and a relation between the transition temperature (T_c) and the composition of the M1 site is apparent: −44 °C in $LiFeSi_2O_6$ (Lottermoser et al. 1998; Redhammer et al. 2001), 13 °C in $LiGaSi_2O_6$ (Sato et al. 1995) and 70 °C in $LiCrSi_2O_6$ (Behruzi et al. 1984). Arlt and Angel (2000) inferred an inverse relation of T_c with the size of the M1 cation. Accordingly, no phase transition could be detected for synthetic $LiScSi_2O_6$ and $LiInSi_2O_6$ clinopyroxenes, which host larger M1 cations. Because the ionic radius of Al^{3+} is shorter than that of Cr^{3+} (0.535 vs. 0.615 Å; Shannon 1976), spodumene ($LiAlSi_2O_6$, the only Li-clinopyroxene occurring in nature), should have the $P2_1/c$ space group at least up to 100 °C. On the contrary, spodumene has the $C2/c$ space group at room temperature and pressure, and also shows a unique S-rotation of the chains of tetrahedra. Moreover, the stability field of spodumene is a function of pressure, the $P2_1/c$ space group being stable at room temperature at pressures >3.19 GPa (Arlt and Angel 2000).

Further information on the $P2_1/c \rightarrow C2/c$ phase transition has been obtained from Fe–Mg low-Ca pyroxenes [pigeonites, ^{M2}(Fe,Mg,Ca) ^{M1}(Fe,Mg) Si_2O_6]. The available data show a direct relation between the

composition and the transition temperature (Prewitt et al. 1971; Brown et al. 1972; Sueno et al. 1984; Arlt and Armbruster 1997; Arlt et al. 2000; Tribaudino 2000). In particular, Arlt et al. (2000) proposed that T_c depends on the aggregate ionic radius of the M2 cations ($\langle$i.r.$\rangle_{M2}$).

Partial chemical substitutions at both the octahedral sites are thus expected to affect the $P2_1/c \rightarrow C2/c$ transition temperature in clinopyroxenes in a rather complex way. In order to understand this feature, we synthesized a clinopyroxene sample with significant $MgLi_{-1}$ and $MgFe^{3+}_{-1}$ substitution with respect to $LiFeSi_2O_6$. This latter clinopyroxene had been named Li-aegirine by Redhammer et al. (2001) and references therein; however, it is an alkaline pyroxene according to Morimoto (1989), and must thus be named ferrian spodumene.

The amount of Mg occurring at M1 is constrained by electroneutrality to be equal to that occurring at M2. The effects on T_c due to the presence of Mg should be opposite; at the M1 site, the increase in the aggregate ionic radius (i.r.$_{Mg} = 0.72$ Å, i.r.$_{Fe^{3+}} = 0.645$ Å: Shannon 1976) should lower T_c, whereas at the M2 site the decrease in the aggregate ionic radius (i.r.$_{Li} = 0.76$ Å: Shannon 1976) should increase T_c.

Experimental methods

Synthesis

High-grade commercial reagent products were used as starting materials. MgO, Fe_2O_3 and SiO_2 oxides were dried at 200 °C and hydrate lithium-hydroxide ($LiOH \times H_2O$) was dried at 70 °C for 24 h. MgO, Fe_2O_3 and $LiOH \times H_2O$ were mixed in stoichiometric amounts and blended by hand in an agate mortar for 60 min. A double-chamber arrangement of the load was prepared by pinching the gold capsule at half height, following the procedure described by von Goerne et al. (1999, 2000), so that only a small passage is available for the fluid phase. The mixture of $LiOH \times H_2O$, MgO, Fe_2O_3 and the fluid phase was placed in the first chamber, and SiO_2 was placed in the second chamber with a 5 wt% stoichiometric excess to prevent the loss of silica in the fluid phase. A LiBr 2M aqueous solution with a fluid/solid ratio of 130 wt% was used, which determined Li excess in the system. The presence of a large amount of fluid phase and this charge design, which develops a chemical gradient, limit nucleation and promote the growth of large crystals. To increase crystal size, the run temperature was also decreased (three times per day) by 40 °C from the run temperature of 700 °C for a duration of 1 h (von Goerne et al. 1999, 2000).

The experiment was carried out in a standard cold seal pressure vessel (CSPV) made with an Ni-rich alloy, operating horizontally, which was kept at a pressure of 0.4 GPa for a duration of 7 days. The temperature was continuously recorded with a K-type calibrated thermocouple approaching the operative hot zone (± 10 °C accuracy). The pressure medium was pure argon, and the pressure was monitored with a strain-gauge manometer (± 5 MPa accuracy). The intrinsic redox state of the vessel was around NNO + 2.3, as previously measured by a solid fO_2 redox sensor (Berndt et al. 2001). Quenching was done by removing the furnace and cooling the vessel with fresh compressed air, with a quench drop rate around 50 °C min^{-1}. At the end of the run, the capsule was reweighted to check for possible leaks and then opened. The run product was separated in a Teflon microfilter and washed with bidistilled water. It consisted in brown crystals ca. 100 μm long. Single crystals were selected by checking optical properties and X-ray diffraction behaviour.

In situ heating experiments

Crystal 301 n. 3 was selected for X-ray data collection at different temperatures. In situ annealing was done using a microfurnace built specifically for the Philips PW1100 four-circle diffractometer at the Department of Earth Sciences of the University of Cambridge. This furnace allows working temperatures up to 1100 °C and data collection in the 2θ range 3–58°.

The crystal was put in a sealed quartz vial (1 mm Ø) together with some graphite powder; some quartz wool kept the crystal steady and avoided mechanical stress. Graphite-monochromatized Mo $K\alpha$ X-radiation and working conditions of 55 kV and 30 mA were used for crystal analysis and data collection.

The space group observed at room temperature is $P2_1/c$. After each annealing step (Table 1), lattice parameters were measured by centring 24 selected *hkl* *a*-type reflections ($h + k = 2n$), and the intensities of five *hkl* *b*-type reflections ($h + k = 2n + 1$) (namely, 102, 052, $\bar{7}02$, $\bar{2}\bar{3}3$, $\bar{2}33$) were monitored (ω-rotations and step-scan profiles recorded with a scan width of 3°). Intensities were scaled with respect to those of adjacent *a*-type reflections in the same reciprocal row (202, 062, $\bar{6}02$, $\bar{1}\bar{3}3$, $1\bar{3}3$). This procedure allowed detection of the temperature of transition via a careful inspection of the intensity of *b*-type reflections and of the shape of their profiles.

Data collection and structure refinement

Room-temperature diffracted intensities were first collected in the θ range 2–35° before mounting the microfurnace. During in situ annealing, data collections were done at 70, 95, 125, 150 and 200 °C by measuring two equivalent monoclinic reflections (*hkl* and $h\bar{k}l$) in the θ range 2–28°. Profiles were integrated following the method of Lehmann and Larsen (1974) modified by Blessing et al. (1974). Intensities were corrected for Lorentz and polarization factors, and for absorption following North et al. (1968). After each data collection, unit-cell dimensions were calculated from least-squares refinement of the centroid of the reflections in the range $-35 < \theta < 35°$ measured for ~50 different rows of the reciprocal space at room temperature and for ~40 rows at higher temperatures. Weighted structure refinements were done with SHELXL-97 (Sheldrick 1997) using all the collected reflections. Scattering curves for fully ionized chemical species were used at those sites where chemical substitutions occur (i.e., M1 and M2); neutral vs. ionized scattering curves were used for Si at the tetrahedral and for O at the anion sites (Hawthorne et al. 1995). Scattering factors were taken from the International Tables for Crystallography (1992). Crystallographic details are reported in Table 2. Positional and isotropic displacement parameters are reported in Table 3, anisotropic displacement parameters are reported in Table 4 (deposited) and selected bond distances and angles are reported in Table 5. Observed and calculated structure factors are reported in Table 6 (deposited).

Electron and ion microprobe analyses

After in situ annealing, the crystal was embedded in epoxy resin and polished. Analyses were done with an ARL-SEMQ electron microprobe (EMP) equipped with four spectrometers (TAP, PET, LiF200 and ADP crystals) at the Dipartimento di Scienze della Terra, Università di Modena, using minerals as standards. Analytical conditions were: 15 kV accelerating potential, 20 nA beam current, 3 μm spot size, 20 s counting times. The $\phi(\rho z)$ correction was applied (Armstrong 1988).

Ion microprobe analyses for Li were done with a Cameca IMS 4f ion microprobe installed at IGG-Pavia. A $^{16}O^-$ primary ion beam with 2–5 nA current intensity was used, and $^7Li^+$ and $^{30}Si^+$ isotopes were monitored as secondary positive ions with medium–high emission kinetic energies in the range ~75–125 eV. The SiO_2 values (wt%), used as inner references for SIMS quantification, were those derived by EMPA. Quantification

Table 1 Refined unit-cell parameters, principal axes ($\times 10^{-3}$) of the strain ellipsoid, the angle between ε_1 and the *a* edge scalar strain ($\times 10^{-3}$), and the ordering parameter ($\Sigma I_a/\Sigma I_b$) measured for ferrian magnesian spodumene

T (°C)	*a* (Å)	*b* (Å)	*c* (Å)	β (°)	*V* (Å)^3	ε_1	ε_2	ε_3	$\varepsilon_1 \hat{} a$ (°)	ε_{ss}	$\Sigma I_b/\Sigma I_a$
25	9.645 (6)	8.713 (3)	5.268 (2)	109.88 (3)	416.3 (3)	−0.9	2.7	−8.4	57.0	10.2	0.186
37	9.645 (6)	8.712 (3)	5.271 (3)	109.88 (4)	416.5 (4)	−0.7	2.5	−8.2	59.4	9.8	0.189
40	9.645 (7)	8.714 (3)	5.270 (3)	109.87 (5)	416.6 (4)	−0.7	2.7	−8.4	58.6	10.1	0.183
45	9.647 (7)	8.714 (4)	5.272 (2)	109.89 (3)	416.8 (4)	−0.7	2.6	−8.0	59.5	9.6	0.180
50	9.649 (9)	8.714 (4)	5.271 (3)	109.89 (4)	416.8 (5)	−0.7	2.6	−8.0	57.9	9.6	0.174
55	9.652 (8)	8.715 (3)	5.273 (2)	109.92 (4)	417.0 (4)	−0.8	2.6	−7.5	58.5	9.0	0.165
60	9.655 (6)	8.713 (4)	5.275 (3)	109.93 (4)	417.2 (4)	−0.6	2.4	−7.1	58.9	8.6	0.156
65	9.653 (7)	8.714 (4)	5.275 (3)	109.93 (4)	417.1 (4)	−0.7	2.4	−7.3	59.9	8.7	0.150
70	9.655 (5)	8.713 (4)	5.280 (2)	109.95 (6)	417.5 (4)	−0.3	2.3	−6.7	63.7	7.9	0.138
75	9.658 (8)	8.710 (3)	5.283 (3)	110.00 (5)	417.6 (5)	−0.5	1.9	−6.0	66.6	7.0	0.126
80	9.659 (11)	8.706 (7)	5.283 (5)	109.97 (7)	417.5 (7)	−0.1	1.4	−6.2	65.1	7.1	0.116
85	9.663 (9)	8.706 (6)	5.286 (4)	109.99 (5)	417.9 (6)	0.1	1.3	−5.6	66.6	6.5	0.099
90	9.666 (10)	8.704 (7)	5.290 (5)	109.99 (6)	418.2 (7)	0.7	1.0	−5.2	68.8	6.0	0.087
95	9.686 (10)	8.699 (8)	5.293 (5)	110.11 (8)	418.8 (7)	0.3	0.4	−2.9	65.5	3.4	0.074
100	9.699 (9)	8.695 (4)	5.294 (5)	110.21 (7)	419.0 (6)	−0.4	−0.1	−1.5	53.0	1.7	0.063
105	9.699 (6)	8.698 (5)	5.298 (4)	110.22 (6)	419.4 (5)	0.0	0.2	−1.2	74.3	1.3	0.052
110	9.702 (6)	8.696 (5)	5.296 (4)	110.25 (6)	419.2 (5)	−0.6	−0.1	−0.9	55.1	1.1	0.044
115	9.703 (7)	8.697 (5)	5.297 (4)	110.22 (7)	419.5 (5)	−0.1	0.0	−1.0	58.3	1.2	0.037
120	9.705 (7)	8.697 (5)	5.297 (4)	110.26 (6)	419.4 (5)	−0.5	−0.1	−0.7	32.1	0.9	0.027
125	9.707 (7)	8.697 (5)	5.298 (4)	110.25 (5)	419.6 (5)	−0.3	−0.1	−0.6	42.7	0.7	0.025
130	9.708 (7)	8.698 (6)	5.298 (4)	110.24 (4)	419.7 (5)	−0.1	−0.1	−0.6	41.3	0.7	0.018
135	9.711 (5)	8.698 (5)	5.301 (3)	110.26 (4)	420.1 (4)						0.016
141	9.712 (6)	8.699 (4)	5.302 (5)	110.27 (6)	420.2 (5)						0.007
150	9.713 (7)	8.702 (4)	5.301 (3)	110.26 (5)	420.3 (5)						0.006
160	9.716 (5)	8.702 (5)	5.302 (3)	110.28 (4)	420.5 (4)						0.003
170	9.716 (5)	8.702 (5)	5.302 (3)	110.28 (4)	420.5 (4)						
180	9.714 (5)	8.700 (5)	5.301 (3)	110.25 (0)	420.3 (4)						
190	9.714 (5)	8.704 (4)	5.301 (3)	110.23 (4)	420.5 (4)						
200	9.714 (6)	8.704 (4)	5.302 (3)	110.24 (5)	420.6 (4)						
225	9.715 (5)	8.707 (4)	5.304 (3)	110.25 (5)	420.9 (4)						
250	9.718 (3)	8.709 (3)	5.305 (3)	110.23 (3)	421.3 (3)						
300	9.720 (6)	8.712 (4)	5.306 (3)	110.22 (3)	421.6 (4)						
350	9.724 (6)	8.717 (4)	5.308 (3)	110.24 (4)	422.2 (4)						
400	9.728 (5)	8.721 (3)	5.307 (3)	110.19 (3)	422.6 (4)						
450	9.728 (5)	8.726 (5)	5.309 (2)	110.20 (3)	423.0 (4)						
500	9.732 (6)	8.732 (4)	5.309 (2)	110.18 (4)	423.5 (4)						

was obtained on the basis of a calibration line for Li/Si in silicates (Ottolini et al. 1993). The estimated accuracy is around ±10%.

Oxide wt% and unit formulae calculated on the basis of 2 Si per formula unit (pfu) are reported in Table 7. Combination of chemical analyses, refined site scatterings and mean bond distances measured at the M1 and M2 sites allowed calculation of the crystal-chemical formula, and in particular of the partitioning of Mg and Fe^{2+}: $^{M2}(Li_{0.85}Mg_{0.09}Fe^{2+}_{0.06})\ ^{M1}(Fe^{3+}_{0.85}Mg_{0.15})Si_2O_6$.

Results

Lattice parameters

The evolution of lattice parameters with temperature is reported in Fig. 1. The *a* and *c* edges, as well as the unit-cell volume, lengthens abruptly from room temperature to 106 °C, and slowly and linearly at higher temperatures. The monoclinic angle β increases from room temperature to 106 °C, and decreases slowly with further heating. The *b* edge lengthens from room temperature to 75 °C, shortens abruptly from 75 to 106 °C, and lengthens linearly at higher temperatures. A similar evolution of the lattice parameters has been observed in many synthetic clinopyroxenes (ferrian spodumene: Redhammer et al. 2001, $LiAlGe_2O_6$, $LiCrGe_2O_6$, $LiGaGe_2O_6$, and $LiScGe_2O_6$: M. Behruzi, personal communication, $Ca_{0.15}Mg_{1.85}Si_2O_6$; Tribaudino et al. 2002), as well as in clinohyperstene (Smyth 1974), kanoite (Arlt and Armbruster 1997) and pigeonite (Cámara et al. 2002). Differences concern the temperature ranges and the extent of the kink.

Changes in unit-cell parameters were recorded during both heating (Table 1; black dots in Fig. 1) and cooling experiments (open circles in Fig. 1), and no hysteresis was observed. On the contrary, significant and variable hysteresis had been reported in previous studies (Arlt and Armbruster 1997; Cámara et al. 2002). Linear regression of the data can be obtained only above 130 °C. Therefore, there is a temperature range of ~25 °C above T_c in which non-linear behaviour is observed.

Strain calculations

Strain calculations were done by linear fit of the lattice parameters above 135 °C, and their extrapolation to room temperature according to the tensor analysis

Table 2 Crystal and structure refinement data for the crystal of this work

CNR-IGG identification code		*hom*	*hqj*	*hqh*	*hqm*	*hqk*	*hqf*
T (°C)		25	75	95	125	150	200
Space group		$P2_1/c$	$P2_1/c$	$P2_1/c$	$C2/c$	$C2/c$	$C2/c$
Unit-cell dimensions	*a* (Å)	9.638(3)	9.651(3)	9.672(4)	9.694(3)	9.701(3)	9.707(3)
	b (Å)	8.709(2)	8.706(4)	8.697(4)	8.690(2)	8.690(3)	8.693(2)
	c (Å)	5.258(2)	5.270(2)	5.281(3)	5.293(1)	5.295(2)	5.298(1)
	β (°)	109.83(3)	109.95(3)	110.09(4)	110.23(3)	110.26(3)	110.27(2)
Volume (Å^3)		415.2(3)	416.2(3)	417.2(3)	418.4(3)	418.8(2)	419.4(2)
Crystal size (mm^3)		0.231×0.100×0.165					
Theta range for data collection		2.2–35.0°	2.2–26.5°	2.2–26.6°	3.2–26.5°	3.2–26.5°	3.2–26.5°
Index ranges		$-15\leqslant h\leqslant 14$	$-12\leqslant h\leqslant 11$	$-12\leqslant h\leqslant 11$	$-12\leqslant h\leqslant 11$	$-12\leqslant h\leqslant 11$	$-12\leqslant h\leqslant 11$
		$-14\leqslant k\leqslant 14$	$-10\leqslant k\leqslant 10$	$-10\leqslant k\leqslant 10$	$-10\leqslant k\leqslant 10$	$-10\leqslant k\leqslant 10$	$-10\leqslant k\leqslant 10$
		$0\leqslant l\leqslant 8$	$0\leqslant l\leqslant 6$	$0\leqslant l\leqslant 6$	$0\leqslant l\leqslant 6$	$0\leqslant l\leqslant 6$	$0\leqslant l\leqslant 6$
Reflections collected		3391	1920	1931	967	958	964
Independent reflections		1825	865	873	435	435	437
R(int)		0.023	0.029	0.038	0.027	0.019	0.019
Data/restraints/parameters		1825/0/105	865/0/105	873/0/105	435/0/57	435/0/57	437/0/57
Goodness-of-fit on F^2		1.153	1.109	1.128	1.029	0.991	0.954
Final *R* indices [$I > 2\sigma(I)$]		0.0328	0.0328	0.0326	0.0211	0.0178	0.0174
R indices (all data)		0.0459	0.0572	0.0660	0.0276	0.0244	0.0237

Table 3 Atom coordinates and equivalent isotropic displacement parameters (U_{eq}[a], Å^2) refined at different temperatures for the crystal of this work

CNR-IGG code		*hom*	*hqj*	*hqh*	*hqm*	*hqk*	*hqf*
T (°C)		25	75	95	125	150	200
O1A	*x*	0.8674(2)	0.8672(3)	0.8668(4)	0.1170(2)	0.1169(2)	0.1169(2)
	y	0.3337(2)	0.3340(4)	0.3340(5)	0.0859(2)	0.0858(2)	0.0860(2)
	z	0.1657(3)	0.1629(5)	0.1597(6)	0.1503(3)	0.1505(3)	0.1499(3)
	U_{eq}	0.006(1)	0.005(1)	0.006(1)	0.008(1)	0.008(1)	0.009(1)
O1B	*x*	0.3684(2)	0.3682(4)	0.3675(4)			
	y	0.8353(2)	0.8358(4)	0.8364(5)			
	z	0.1342(3)	0.1372(5)	0.1414(6)			
	U_{eq}	0.007(1)	0.006(1)	0.006(1)			
O2A	*x*	0.1174(2)	0.1176(4)	0.1180(5)	0.3685(2)	0.3682(2)	0.3681(2)
	y	0.5073(2)	0.5079(4)	0.5075(5)	0.2562(2)	0.2564(2)	0.2563(2)
	z	0.3159(3)	0.3184(6)	0.3217(7)	0.3303(4)	0.3297(3)	0.3295(3)
	U_{eq}	0.009(1)	0.009(1)	0.010(1)	0.013(1)	0.013(1)	0.014(1)
O2B	*x*	0.6232(2)	0.6220(4)	0.6203(5)			
	y	1.0006(2)	1.0018(4)	1.0040(5)			
	z	0.3585(3)	0.3518(6)	0.3437(7)			
	U_{eq}	0.009(1)	0.009(1)	0.011(1)			
O3A	*x*	0.1081(2)	0.1077(4)	0.1074(4)	0.3552(2)	0.3550(2)	0.3550(1)
	y	0.2671(2)	0.2643(4)	0.2617(4)	−0.0011(2)	−0.0016(2)	−0.0016(2)
	z	0.5851(3)	0.5819(6)	0.5769(6)	0.0556(3)	0.0561(3)	0.0563(3)
	U_{eq}	0.009(1)	0.008(1)	0.007(1)	0.016(1)	0.014(1)	0.015(1)
O3B	*x*	0.6049(2)	0.6046(3)	0.6040(4)			
	y	0.7205(2)	0.7271(4)	0.7340(5)			
	z	0.5066(3)	0.5161(5)	0.5257(6)			
	U_{eq}	0.010(1)	0.011(1)	0.013(1)			
SiA	*x*	0.0470(1)	0.0467(1)	0.0463(2)	0.2961(1)	0.2959(1)	0.2958(1)
	y	0.3392(1)	0.3392(2)	0.3391(2)	0.0896(1)	0.0898(1)	0.0897(1)
	z	0.2792(1)	0.2771(2)	0.2747(2)	0.2669(1)	0.2670(1)	0.2667(1)
	U_{eq}	0.005(1)	0.004(1)	0.004(1)	0.006(1)	0.006(1)	0.006(1)
SiB	*x*	0.5488(1)	0.5481(1)	0.5473(2)			
	y	0.8386(1)	0.8390(2)	0.8394(2)			
	z	0.2505(1)	0.2535(2)	0.2572(2)			
	U_{eq}	0.005(1)	0.004(1)	0.004(1)			
M1	*x*	0.2502(1)	0.2500(1)	0.2501(1)	0	0	0
	y	0.6480(1)	0.6481(1)	0.6483(1)	0.8985(1)	0.8985(1)	0.8984(1)
	z	0.2340(1)	0.2367(1)	0.2402(2)	1/4	1/4	1/4
	U_{eq}	0.006(1)	0.004(1)	0.005(1)	0.006(1)	0.007(1)	0.008(1)
M2	*x*	0.2520(2)	0.2512(7)	0.2516(9)	0	0	0
	y	0.0139(2)	0.0148(4)	0.0156(5)	0.2664(4)	0.2673(3)	0.2673(3)
	z	0.2314(4)	0.2337(9)	0.237(1)	1/4	1/4	1/4
	U_{eq}	0.015(1)	0.014(1)	0.016(1)	0.018(1)	0.018(1)	0.021(1)

[a] U_{eq} is defined as one third of the trace of the orthogonalized U_{ij} tensor

described in Carpenter et al. (1998). The extrapolated monoclinic angle β was obtained from the equation $\sin\beta = V/(abc)$. The modules of the principal axes of the strain ellipsoid (ε_{1-3}) are reported in Table 1, together with scalar strain (ε_{ss}). Figure 2a reports the evolution as a function of temperature of the components of the strain tensor (e_{ij}) and of the strain volume (V_s), calculated following Carpenter et al. (1998).

Order parameter

Cámara et al. (2002) described the $P2_1/c \rightarrow C2/c$ displacive phase transition in pigeonites as coelastic, which means that the space group changes whereas the point-group symmetry is maintained after the transition. Under this hypothesis, the intensity of *b*-type reflections should be proportional to the square of the macroscopic ordering parameter (Q^2; Carpenter et al. 1998). To minimize errors, the square of the order parameter has been calculated as the ratio of the sum of the intensities of the monitored *a*-type and *b*-type reflections ($\Sigma I_b/\Sigma I_a$; Table 1). The linear correlation between the strain volume and the order parameter [$V_s = -0.035\ (\Sigma I_b/\Sigma I_a)$] confirms the coelastic behaviour. The evolution of the order parameter as a function of temperature (Fig. 2b) consists in a continuous decrease from room temperature to 106 °C, and in a small tail from 106 to 160 °C, indicating that the $P2_1/c \rightarrow C2/c$ phase transition occurs at 106 °C. Beyond 160 °C, *b*-type reflections are

Table 5 Selected interatomic distances (Å) and angles (°) measured at different temperatures for the crystal of this work

CNR-IGG code	*hom*	*hqj*	*hqh*	*hqm*	*hqk*	*hqf*
T (°C)	25	75	95	125	150	200
SiA–O1A	1.629 (2)	1.629 (3)	1.630 (4)	1.630 (2)	1.630 (2)	1.629 (2)
SiA–O2A	1.597 (1)	1.604 (3)	1.603 (5)	1.594 (2)	1.593 (2)	1.593 (2)
SiA–O3A	1.639 (2)	1.646 (3)	1.643 (3)	1.628 (2)	1.629 (2)	1.632 (2)
SiA–O3A	1.629 (1)	1.621 (3)	1.623 (4)	1.626 (2)	1.628 (2)	1.627 (2)
⟨SiA–O⟩	1.623	1.625	1.625	1.619	1.620	1.620
TILT	2.15 (3)	2.30 (4)	2.46 (5)	3.11 (3)	3.07 (3)	3.06 (3)
SiB–O1B	1.637 (2)	1.633 (4)	1.633 (4)			
SiB–O2B	1.597 (1)	1.592 (3)	1.592 (4)			
SiB–O3B	1.634 (2)	1.631 (3)	1.632 (4)			
SiB–O3B	1.634 (2)	1.627 (3)	1.618 (3)			
⟨SiB–O⟩	1.626	1.620	1.619			
TILT	4.25 (3)	4.04 (4)	3.82 (5)			
M1–O1A	2.027 (2)	2.028 (3)	2.030 (4)	2.033 (2)	2.034 (2)	2.032 (2)
M1–O1A	2.142 (1)	2.142 (3)	2.139 (4)	2.152 (2)	2.151 (2)	2.155 (1)
M1–O1B	2.154 (1)	2.157 (3)	2.156 (4)	2.152 (2)	2.151 (2)	2.155 (1)
M1–O1B	2.030 (2)	2.033 (3)	2.036 (4)	2.033 (2)	2.034 (2)	2.032 (2)
M1–O2A	1.924 (1)	1.919 (3)	1.922 (4)	1.926 (2)	1.927 (2)	1.928 (2)
M1–O2B	1.943 (1)	1.939 (3)	1.930 (4)	1.926 (2)	1.927 (2)	1.928 (2)
⟨M1–O⟩	2.037	2.036	2.035	2.037	2.037	2.038
M2–O1A	2.122 (3)	2.123 (6)	2.128 (7)	2.107 (3)	2.113 (3)	2.114 (3)
M2–O1B	2.080 (2)	2.086 (6)	2.081 (7)	2.107 (3)	2.113 (3)	2.114 (3)
M2–O2A	2.137 (3)	2.137 (6)	2.140 (7)	2.154 (2)	2.159 (2)	2.161 (2)
M2–O2B	2.086 (3)	2.114 (6)	2.140 (7)	2.154 (2)	2.159 (2)	2.161 (2)
M2–O3A	2.331 (2)	2.346 (6)	2.367 (6)	2.473 (3)	2.463 (3)	2.464 (3)
M2–O3B	2.804 (3)	2.734 (6)	2.657 (7)	2.473 (3)	2.463 (3)	2.464 (3)
⟨M2–O⟩ × 6	2.260	2.256	2.252	2.245	2.245	2.246
⟨M2–O⟩ × 5	2.151	2.161	2.171	2.199	2.201	2.203
O3A–O3A	2.646 (2)	2.647 (2)	2.649 (2)	2.646 (1)	2.648 (1)	2.649 (1)
O3B–O3B	2.679 (2)	2.665 (2)	2.655 (2)			
O3A–O3A–O3A	192.90 (12)	190.8 (3)	188.8 (3)	179.2 (2)	178.8 (1)	178.8 (2)
O3B–O3B–O3B	157.86 (13)	162.8 (3)	168.0 (3)			

Table 7 Chemical composition of the crystal of this work. The unit formulae were calculated assuming two Si atoms

No. of points	1	2	3	4	5	6	Average	SD
SiO_2	56.47	56.24	55.32	56.07	56.01	56.02	56.02	0.39
Fe_2O_3	31.53	31.55	31.54	31.50	31.54	31.54	31.53	0.02
FeO	2.87	2.34	1.31	2.70	1.49	1.81	2.09	0.65
MgO	4.43	4.88	4.67	3.96	5.45	4.97	4.73	0.51
Li_2O	5.90	5.90	5.90	5.90	5.90	5.90	5.90	0.00
Total	101.20	100.91	98.74	100.13	100.39	100.24	100.27	0.86
Si	2.000	2.000	2.000	2.000	2.000	2.000	2.000	
Mg	0.234	0.259	0.252	0.210	0.290	0.264	0.252	0.03
Fe^{3+}	0.840	0.844	0.858	0.846	0.847	0.847	0.847	0.01
Fe^{2+}	0.085	0.069	0.039	0.081	0.045	0.054	0.062	0.02
Li	0.840	0.844	0.858	0.846	0.847	0.847	0.847	0.01
M1 + M2	1.999	2.016	2.007	1.983	2.029	2.012	2.008	0.02
s.s. M1 (calc)[a]	23.8	23.8	24.0	23.8	23.9	23.9	23.9	
s.s. M2 (calc)	5.6	5.6	4.9	5.3	5.4	5.3	5.3	
s.s. M1 (obs)[b]	23.9	23.9	23.9	23.9	23.9	23.9	23.9	
s.s. M2 (obs)	5.3	5.3	5.3	5.3	5.3	5.3	5.3	
Δ (obs-calc)	0.2	0.2	0.3	0.1	−0.1	0.0	0.0	

[a] s.s. (calc) = electrons per formula unit calculated from EMP analyses
[b] s.s. (obs) = refined site scattering (epfu)

not detectable and thus the crystal has $C2/c$ symmetry. The profiles of *a*-type reflections broaden significantly in the temperature range 70–95 °C, but become sharp again at higher temperature values. Repeated heating and cooling cycles showed the same behaviour. A shrinking of the *b* edge also occurs in the temperature range 70–95 °C (Fig. 1).

The evolution of the order parameter Q below the transition temperature (T_c) can be described through a Landau potential as follows:

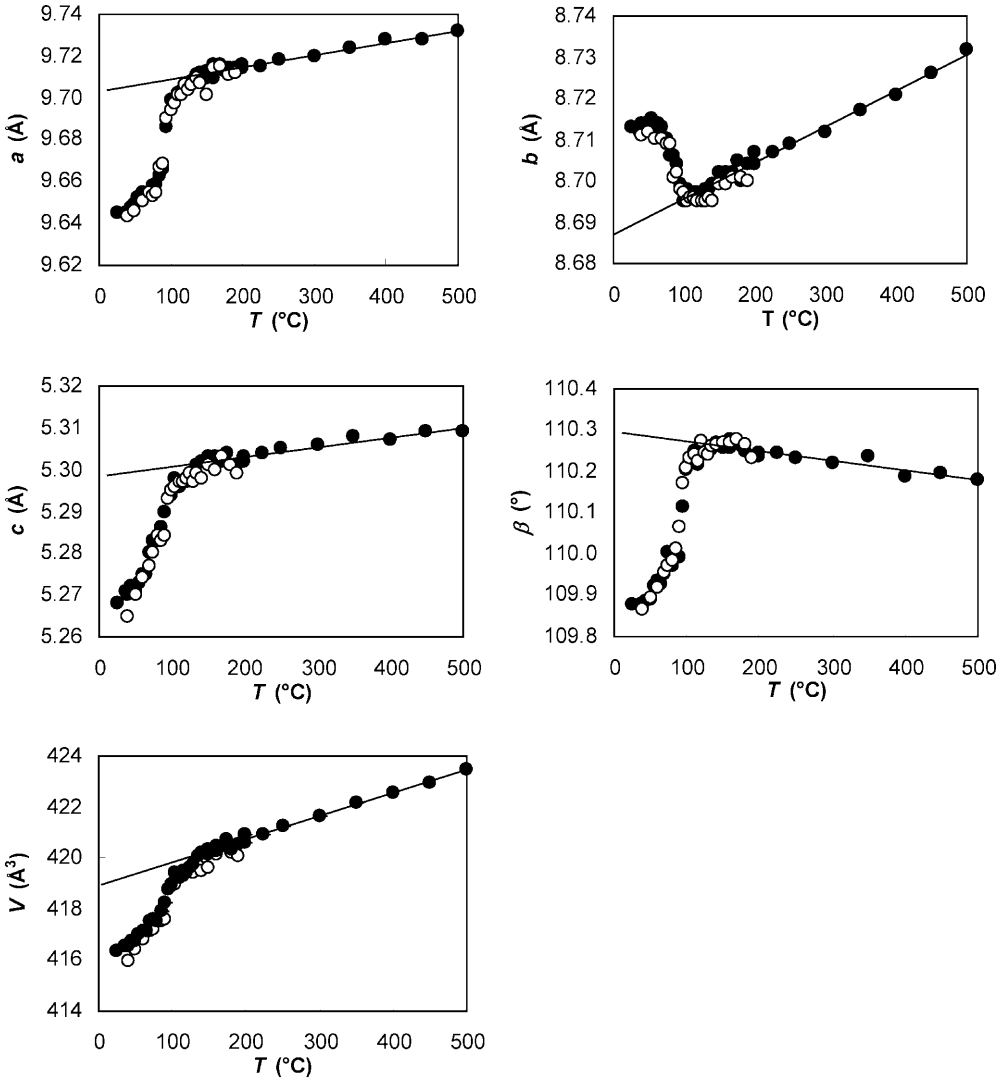

Fig. 1a–e Evolution of the lattice parameters with temperature for the crystal of this work. *Filled dots* heating; *empty dots* cooling cycles. The *line* represents regression of the values measured after the transition for temperatures >130 °C

$$G = \frac{1}{2}a(T - T_c)Q^2 + \frac{1}{4}bQ^4 + \frac{1}{6}cQ^6 \quad (1)$$

At equilibrium

$$\frac{\Delta G}{\partial Q} = 0 = a(T - T_c)Q + bQ^3 + cQ^5 \ ; \quad (2)$$

$$T = T_c - \frac{b}{a}Q^2 - \frac{c}{a}Q^4 \ . \quad (3)$$

Given that $I \propto Q^2$ and using the aggregate intensity ratios measured up to 100 °C, a simple polynomial fit vs. temperature yields $T = 106(5) + 0.2(7.6)Q^2 - 1889(292)Q^4$. The Landau b/a coefficient is small and not significant, and thus the Landau expansion takes the form of a tricritical phase transition.

Structural changes as a function of temperature

The synthetic clinopyroxene of this work, with crystal-chemical composition $^{M2}(Li_{0.85}Mg_{0.09}Fe^{2+}_{0.06})$ $^{M1}(Fe^{3+}_{0.85}Mg_{0.15})Si_2O_6$, has $P2_1/c$ space group at room temperature. This symmetry implies two independent chains of tetrahedra, the A chain with *S* rotation and the B chain with *O* rotation (Thompson 1970). At room temperature, the geometry of the chains of tetrahedra in this sample is equivalent to that observed in synthetic $LiFeSi_2O_6$ at −173 °C, i.e., well apart from the transition temperature (Redhammer et al. 2001). For instance, the O3–O3–O3 angles (where O3 is the oxygen atom bridging the tetrahedra) are 192.55(2)° and 192.9(2)° for the A chain and 160.02(7)° and 158.0(2)°, respectively, for the B chain in $LiFeSi_2O_6$ at −173 °C and in the crystal of this work at room temperature. Thus, the overall effect of the entrance of Mg (and Fe^{2+}) in the structure of ferrian spodumene is nearly equivalent to an increase in temperature of 198 °C.

When approaching the transition temperature, both chains extend along the *c* axis via rotation (kink) of the tetrahedra. Again, this process can be followed by inspection of the O3–O3–O3 angles. Figure 3a compares the O3–O3–O3 values measured for the synthetic crystal of this work (circles) with those reported for

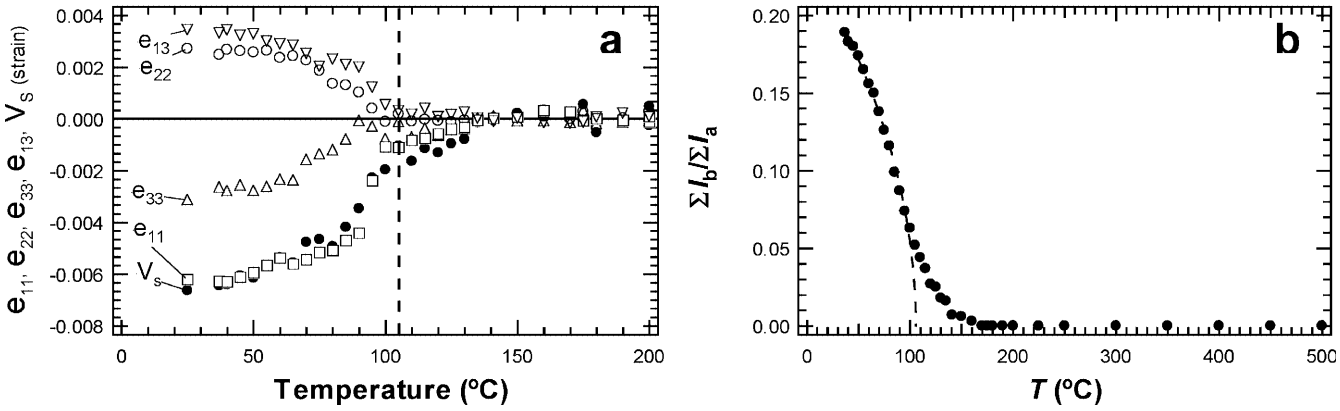

Fig. 2 **a** Variation of the components of the strain tensors and of the strain volume as a function of temperature. **b** Variation of the aggregate intensity ratio between *b*-type reflections (I_b; $h + k = 2n + 1$) and *a*-type reflections (I_a; $h + k = 2n$). The *dashed line* represents the polynomial fit to the experimental data in terms of a 246 Landau expansion

synthetic magnesian clinoferrosilite (crosses: Smyth 1974), kanoite (triangles: Arlt and Armbruster 1997), basaltic pigeonite (diamonds: Cámara et al. 2002) and synthetic Ca-rich clinoenstatite (squares: Tribaudino et al. 2002). In synthetic ferrian magnesian spodumene, the *S*-rotated A chain stretches by 4°, whereas the *O*-rotated B chain stretches by 10° from room *T* to 95 °C. After the transition, the unique chain of tetrahedra is *O*-rotated and nearly fully extended (179.2°), similarly to synthetic ferrian spodumene. An analogous behaviour is observed for all the other compositions reported in Fig. 3a, except for the basaltic pigeonite, in which the two O3–O3–O3 angles smoothly approach convergence.

The out-of-plane tilting of the basal face of the tetrahedra (TILT) is also useful to monitor the transition (Fig. 3b). In synthetic ferrian magnesian spodumene, the TILT values tend to decrease even beyond the transition. In the $P2_1/c$ stability field of the other pyroxenes, either continuous (pigeonite) or discontinuous (kanoite) behaviour is observed.

Focusing on the individual structural sites, the M1 site is larger in synthetic ferrian magnesian spodumene than in synthetic ferrian spodumene ($\langle$M1–O$\rangle = 2.037$ vs. 2.024 Å, respectively, at room temperature) because of the presence of divalent cations (i.r.$_{Mg} = 0.72$ Å, i.r.$_{Fe^{2+}} = 0.78$ Å, i.r.$_{Fe^{3+}} = 0.645$ Å: Shannon 1976). At the M2 site, the coordination geometry is similar in the two samples. However, the M2–O2A distance is shorter in the synthetic crystal of this work due to the presence of a cation (Mg) smaller than Li (i.r.$_{Li} =$ 0.76 Å: Shannon 1976).

The M2 site has a fivefold coordination in the low-temperature $P2_1/c$ structure, and a sixfold coordination

Fig. 3a, b Changes in the conformation of the chains of tetrahedra as a function of temperature. **a** Kinking, measured by the O3–O3–O3 angle. **b** Out-of-plane tilting (*TILT*). *Circles* A-chain values; *dots* B-chain values; *crosses* synthetic magnesian clinoferrosilite (Smyth 1974); *triangles* kanoite (Arlt and Armbruster 1997); *squares* synthetic Ca-rich clinoenstatite (Tribaudino et al. 2002); *diamonds* pigeonite (Cámara et al. 2002)

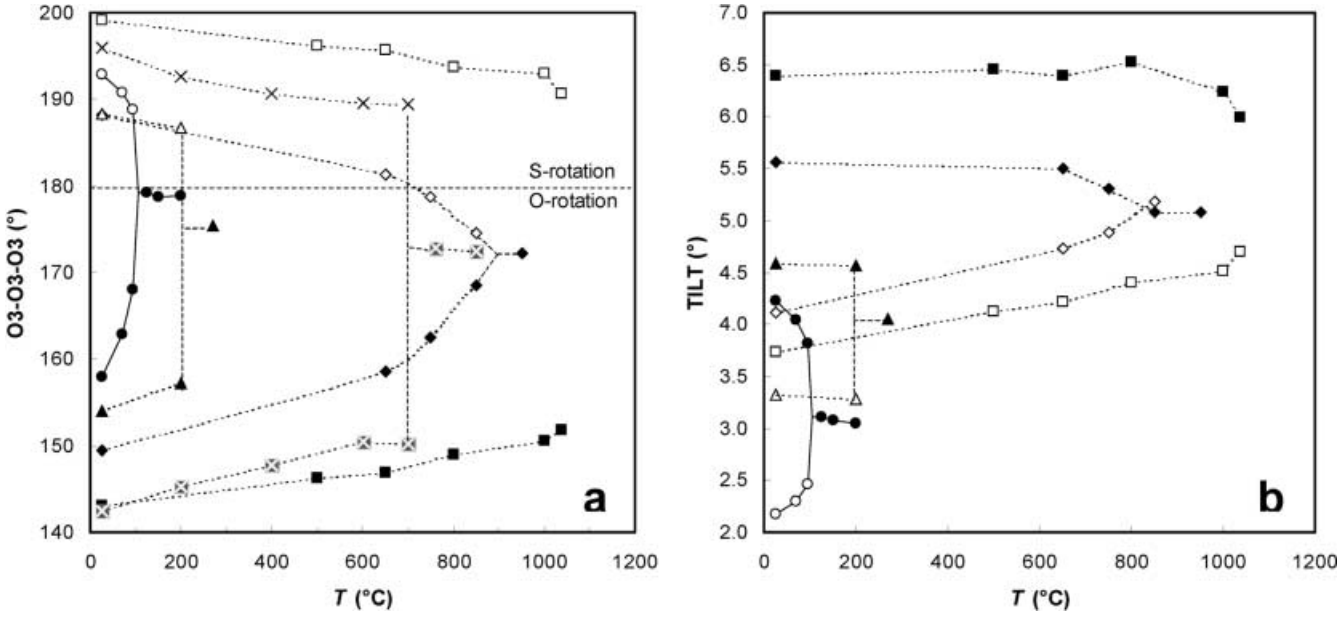

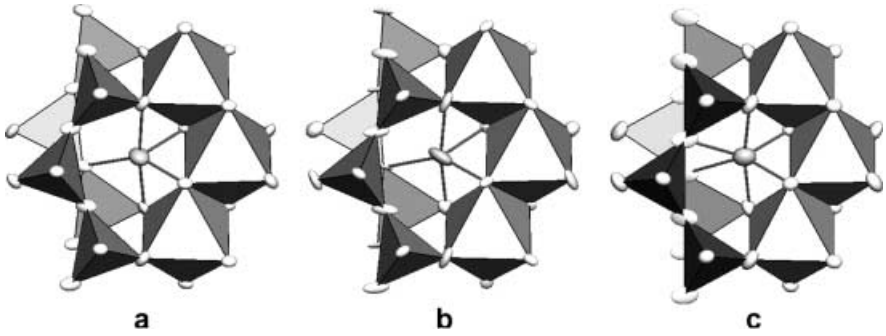

Fig. 4a–c Changes in the shape of the anisotropic displacement parameters at M2 and in M2 coordination observed in synthetic ferrian magnesian spodumene as a function of temperature. **a** 25 °C; **b** 95 °C; **c** 125 °C. Bond interactions shorter than 2.5 Å are shown as *sticks*, and the *ellipsoids* are drawn at 95% probability. While the temperature approaches T_c (i.e., 106 °C), the ellipsoid elongates in the direction of the approaching O3B oxygen due to the stretching of the B chain; the shape turns into regularity after the transition, when coordination is sixfold

in the high-temperature $C2/c$ structure. With increasing temperature, the kinking of the B chain decreases, and O3B approaches M2 (2.657 Å at 95 °C), giving rise to an incipient bonding interaction, which is complete after the transition (2.473 Å at 125 °C). The same process can be followed by considering changes in the shape of the anisotropic displacement parameters measured at the M2 site (Fig. 4). When approaching T_c, the ellipsoid becomes strongly anisotropic, with the major component in the direction of the approaching O3B oxygen. After the displacive phase transition, a new bond is formed between M2 and O3B, and the displacement ellipsoid is far more regular, with the longest component parallel to the *b* axis.

Discussion

The high-pressure $P2_1/c \rightarrow C2/c$ phase transition in spodumene and in synthetic $LiScSi_2O_6$ has been studied by Arlt and Angel (2000), who found that it is first-order in the former and second-order in the latter. On the contrary, the thermodynamic character of the high-temperature phase transition in Li-clinopyroxenes has not yet been systematically investigated.

The data reported in this work for the displacive $P2_1/c \rightarrow C2/c$ phase transition in synthetic $^{M2}(Li_{0.85}Mg_{0.09}Fe^{2+}_{0.06})\ ^{M1}(Fe^{3+}_{0.85}Mg_{0.15})Si_2O_6$ can be directly compared with those reported for synthetic ferrian spodumene (Lottermoser et al. 1998; Redhammer et al. 2001), which were obtained by cooling experiments. The entrance of 0.15 Mg (and Fe^{2+}) apfu in the M1 and in the M2 sites increases the transition temperature (T_c) by 151 °C. Arlt and Angel (2000) inferred an inverse relation between T_c and the size of the M1 cation. In the crystal of this work, the aggregate ionic radius is at M1 0.011 Å longer than in synthetic ferrian spodumene ($<$i.r.$>_{M1} = 0.656$ Å; i.r.$_{Mg} = 0.72$ Å, i.r.$_{Fe^{3+}} = 0.645$ Å: Shannon 1976), and the transition temperature should thus be lower. Therefore, the presence of 0.15 apfu of divalent cations at the M2 site, which changes its aggregate ionic radius by only 0.002 Å ($<$i.r.$>_{M2} = 0.758$ Å; i.r.$_{Fe^{2+}} = 0.78$; i.r.$_{Li} = 0.76$ Å: Shannon 1976), is likely to affect thermodynamic behaviour more strongly than that at the M1 site. The effect of solid solution at the M2 site in pigeonite has been discussed by Arlt et al. (2000) and Cámara et al. (2002). However, reliable models of the changes in T_c vs. the aggregate ionic radii cannot be provided because most of the data available in the literature do not report detailed site populations. Models should, in principle, be constructed starting from the available mean bond lengths; however, the actual site population and changes in charge distribution due to heterovalent substitutions are important factors to be considered.

We observed a significant peak broadening below T_c, specifically in the temperature range 70–95 °C, which is concomitant with a shortening of the *b* edge (Fig. 1b). This evidence can be explained by local development of highly strained areas, which disappear after the phase transition. Also the strongly anisotropic displacement parameters observed at the M2 site when approaching T_c (Fig. 4) can be interpreted as heterogeneities related to the solid solution, because the larger Fe^{2+} and Li^{+} cations can increase their coordination number at the

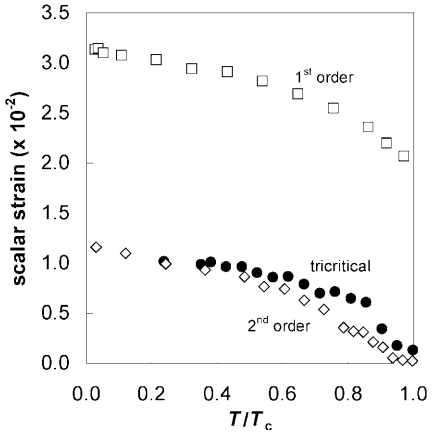

Fig. 5 Changes in the scalar strain observed for three different compositions with distinct thermodynamic behaviour. Symbols as in Fig. 3

expense of the approaching O3B oxygen well before the smaller Mg^{2+} cation. After the $P2_1/c \rightarrow C2/c$ phase transition, the structure can relax, and the shape of the electron density becomes more isotropic.

As discussed above, the $P2_1/c \rightarrow C2/c$ phase transition in ferrian magnesian spodumene is coelastic (i.e., the spontaneous strain scales with the strain volume) and tricritical. Actually, it is the first case of a tricritical behaviour reported for the HT displacive phase transition in clinopyroxenes. Other compositions observe either first-order (Smyth 1974; Arlt and Armbruster 1997; Tribaudino et al. 2002) or second-order behaviour (Cámara et al. 2002). These latter authors also provided evidence that the character of the transition mainly depends on the M2 site composition. The presence of microstructures has also been proposed to be a non-negligible factor (Tribaudino et al. 2002).

Based on the available evidence, a term related to composition should be included in the square term of the free-energy Landau expansion which describes the behaviour of clinopyroxene solid solutions. Also, the coefficient of the Q^4 term of the Landau expansion, which is related to the character of the phase transition, should now be expected to vary with composition and even to change sign from negative (discontinuous phase transition), to 0 (tricritical), to positive (continuous phase transition). If this is true, all the cases in which $b/a > 0$ will be better described by means of a 246 Landau expansion. The observed dependence on composition of the coefficient of the Q^4 term of the expansion implies the existence of a subtractive coupling term related to spontaneous strain. This term must also be a function of composition, and should imply high values of both scalar and volume strain in Fe-free pigeonite (Tribaudino et al. 2002) but low values in Fe-rich pigeonite (Cámara et al. 2002; Fig. 5). Because the $P2_1/c \rightarrow C2/c$ phase transition is a zone-boundary transition, only quadratic coupling is allowed for strain due to symmetry constraints (Salje 1990). The Landau expansion would then take the form:

$$G = \frac{1}{2}a\left(T - T_c - \frac{2\lambda X}{a}\right)Q^2 + \frac{1}{4}\left(b - \frac{\lambda e^2}{f}\right)Q^4 + \frac{1}{6}cQ^6 + \cdots$$

with the term λX representing the coupling with composition, λe the coupling with strain, and f the elastic energy coefficient.

Acknowledgements Luisa Ottolini (IGG-Pavia) is gratefully acknowledged for ion microprobe analysis of Li. The synthesis described in this work was done during the stay of G.I. at the Institut für Mineralogie of the Universität Hannover, for which financial support by EGIDE–Italian Minister of Foreign Affairs is acknowledged. François Holtz, Harald Behrens and their staff are gratefully thanked for help and supervision. The Consiglio Nazionale delle Ricerche provided funding for the electron microprobe laboratory in Modena University as well as for the ion microprobe laboratory at IGG-Pavia (formerly CSCC).

References

Armstrong JT (1988) Quantitative analysis of silicates and oxide minerals: comparison of Monte-Carlo, ZAF and Phi-Rho-Z procedures. Microbeam Anal: 239

Arlt T, Armbruster T (1997) The temperature-dependent $P2_1/c$–$C2/c$ phase transition in the clinopyroxene kanoite $MnMg[Si_2O_6]$: a single-crystal X-ray and optical study. Eur J Mineral 9: 953–954

Artl T, Angel RJ (2000) Displacive phase transitions in C-centred clinopyroxenes: spodumene, $LiScSi_2O_6$ and $ZnSiO_3$. Phys Chem Miner 27: 719–731

Arlt T, Kunz M, Stolz J, Ambruster T, Angel RJ (2000) P–T–X data on $P21/c$ clinopyroxenes and their displacive phase transitions. Contrib Mineral Petrol 138: 35–45

Berndt J, Holtz F, Koepke J (2001) Experimental constraints on storage conditions in the chemically zoned phonolitic magma chamber of the Laacher See volcano. Contrib Mineral Petrol 140: 469–486

Behruzi M, Hahn Th, Prewitt CT, Baldwin K (1984) Low- and high-temperature crystal structures of $LiFeGe_2O_6$, $LiFeSi_2O_6$ and $LiCrSi_2O_6$. Acta Crystallogr (A) 40: C–247

Blessing RH, Coppens P, Becker P (1974) Computer analysis of step-scanned X-ray data. J Appl Crystallogr 7: 488–492

Brown GE, Prewitt CT, Papike JJ, Sueno S (1972) A comparison of the structures of low and high pigeonite. J Geophys Res 77: 5778–5789

Cámara F, Carpenter MA, Domeneghetti MC, Tazzoli V (2002) Non-convergent ordering and displacive phase transition in pigeonite: in-situ HT XRD study. Phys Chem Miner 29: 331–340

Carpenter MA, Salje EKH, Graeme-Barber A (1998) Spontaneous strain as a determinant of thermodynamic properties for phase transition in minerals. Eur J Mineral 10: 621–691

Goerne von G, Franz G (2000) Synthesis of Ca-tourmaline in the system CaO–MgO–Al_2O_3–SiO_2–B_2O_3–H_2O–HCl. Mineral Petrol 69: 161–182

Goerne von G, Franz G, Wirth R (1999) Hydrothermal synthesis of large dravite crystals by the chamber method. Eur J Mineral 11: 1061–1077

Hawthorne FC, Ungaretti L, Oberti R (1995) Site populations in minerals: terminology and presentation of results of crystal-structure refinement. Can Mineral 33: 907–911

International Tables for crystrallopgraphy vol e. (1992), Wilson AJC (ed), Kluwer Acadamic Publishers, Dordrecht Boston London

Lehmann MS, Larsen FK (1974) A method for location of the peaks in step-scan-measured Bragg reflections. Acta Crystallogr (A) 30: 580–584

Lottermoser W, Redhammer G, Forcher K, Amthauer G, Paulus W, André G, Treutmann W (1998) Single crystal Mössbauer and neutron powder diffraction measurements on the synthetic clinopyroxene Li-acmite $LiFeSi_2O_6$. Z Kristallogr 213: 101–107

Morimoto N (1989) Nomenclature of pyroxene. Subcommittee on pyroxenes. Can Mineral 27: 143–156

North ACT, Phillips DC, Mathews FS (1968) A semi-empirical method of absorption correction. Acta Crystallogr (A) 24: 351–359

Ottolini L, Bottazzi P, Vannucci R (1993) Quantification of lithium, beryllium, and boron in silicates by secondary ion mass spectrometry using conventional energy filtering. Anal Chem 65: 1960–1968

Prewitt CT, Brown GE, Papike JJ (1971) Apollo 12 clinopyroxenes. High-temperature X-ray diffraction studies. Geochim Cosmochim Acta, Suppl 2, 1: 59–68

Redhammer GJ, Roth G, Paulus W, André G, Lottermoser W, Amthauer G, Treutmann W, Koppelhuber-Bitschnau B (2001) The crystal and magnetic structure of Li-aegirine $LiFeSi_2O_6$: a temperature-dependent study. Phys Chem Miner 28: 337–346

Salje EKH (1990) Phase transition in ferroelastic and co-elastic crystals, 1st edn. Cambridge University Press, Cambridge, UK pp 366

Sato A, Osawa T, Ohashi H (1995) Low temperature from of $LiGaSi_2O_6$. Acta Crystallogr (C) 51: 1959–1960

Shannon RD (1976) Revised affective ionic radii and systematic studies of interatomic distances in halides and chalcogenides. Acta Crystallogr (A) 32: 751–767

Sheldrick GM (1997) Programs for crystal structure analysis (release 97–2). Institut für anorganische Chemie der Universität, Tammanstrasse 4, 3400 Göttingen, Germany, 1998

Smyth JR (1974) The high-temperature crystal chemistry of clinohypersthene. Am Mineral 59: 1069–1082

Sueno S, Kimata M, Prewitt CT (1984) The crystal structure of high clinoferrosilite. Am Mineral 69: 264–269

Thompson JB Jr (1970) Geometrical possibilities for amphiboles structures: model biopyriboles. Am Mineral 55: 292–293

Tribaudino M (2000) A transmission electron microscope investigation of the $C2/c \rightarrow P2_1/c$ phase transition in clinopyroxenes along the diopside–enstatite ($CaMgSi_2O_6$–$Mg_2Si_2O_6$) join. Am Mineral 85: 707–715

Tribaudino M, Nestola F, Cámara F, Domeneghetti MC (2002) The high-temperature $P2_1/c \rightarrow C2/c$ phase transition in Fe-free pyroxenes: structural and thermodynamic behavior. Am Mineral 87: 648–657